water

MDPI

Article

Effects of Chemical Activation Conditions on Hierarchical Porous Carbon via Oxytetracycline Adsorption

Fernando Oscar Hayrera [1], Do-Gun Kim [2,*] and Seok-Oh Ko [1,*]

[1] Department of Civil Engineering, Kyung Hee University, 1732 Deogyeongdaero, Yongin 17104, Republic of Korea; fernandooscar@khu.ac.kr
[2] Department of Environmental Engineering, Sunchon National University, 255 Jungangro, Suncheon 57922, Republic of Korea
* Correspondence: dgkim@scnu.ac.kr (D.-G.K.); soko@khu.ac.kr (S.-O.K.)

Abstract: This study investigated the characteristics and oxytetracycline (OTC) adsorption of hierarchical porous carbons (HPCs) synthesized under different activation conditions using biomass wheat flour (WF) and $NaHCO_3$ as an activator. It was found that the characteristics of the HPCs, such as specific surface area, total and mesopore volume, defects, and crystallinity, were highly dependent on the activation temperature, the dose of the activator, and activation time. In particular, the adsorption mechanisms and adsorption capacity were dominantly governed by the degree of defects in graphitic structures and mesoporosity, which are largely determined by the dose of the activator and the activation temperature. The best OTC adsorption was achieved with the HPC of the most abundant mesopores, which was prepared at 900 °C, a WF:$NaHCO_3$ mass ratio of 1:1, and a duration of 2 h (HPC900_R1.0_2H). Based on the results of the experiments concerning adsorption kinetics, equilibrium adsorption, and the effects of pH, OTC adsorption onto HPC900_R1.0_2H was monolayer in type, homogeneous, governed by the combination of diffusion and chemisorption, and largely attributed to π–π electron–donor–acceptor interactions and electrostatic interactions. The thermodynamic parameters suggest that it is spontaneous and endothermic. These findings provide valuable information about the design and synthesis of HPCs from biomass, which exhibit optimized properties for the adsorption of refractory organic pollutants.

Keywords: hierarchical porous carbon; adsorption; oxytetracycline; activation; thermodynamic

Citation: Hayrera, F.O.; Kim, D.-G.; Ko, S.-O. Effects of Chemical Activation Conditions on Hierarchical Porous Carbon via Oxytetracycline Adsorption. *Water* **2023**, *15*, 3146. https://doi.org/10.3390/w15173146

Academic Editor: Chengyun Zhou

Received: 21 July 2023
Revised: 24 August 2023
Accepted: 25 August 2023
Published: 2 September 2023

1. Introduction

Oxytetracycline (OTC) is a readily available and efficient antibiotic that is used for disease prevention and the growth promotion of livestock and aquaculture [1]. For a significant period of time, a high amount of OTC has been discharged into the environment, resulting in negative consequences on aquatic ecosystems, including detrimental changes in microbial community structures and the spread of antibiotic-resistant bacteria and genes [2,3]. Moreover, conventional wastewater treatment plants (WWTPs) cannot effectively remove OTC from water due to its recalcitrant characteristics [1,2,4].

Several alternatives have been tried in attempts to remove OTC in aqueous environments, such as photolysis, advanced oxidation processes (AOPs), hydrolysis, and ozonation. However, they have several drawbacks: photolysis only degrades compounds that are photosensitive, and the reaction is relatively slow at environmental temperatures; AOPs have poor selectivity and the metals employed to achieve high removal efficiency can be leached, thus causing secondary pollution; hydrolysis is easily affected by the pH and temperature of the solution; and more toxic byproducts can be formed by ozonation [5–8].

It has been established that the safest and most efficient method to remove OTC from water is through adsorption using carbon-based adsorbents [9]. Adsorption has been extensively employed in the treatment of antibiotic wastewater due to the benefits of

convenient operation, low cost, high efficiency, and the absence of toxic byproducts, without a reaction between an adsorbate (i.e., pollutant) and an adsorbent [10]. Carbon-based functional materials have recently been given great attention for a variety of applications, such as the removal of water pollutants, application as a catalyst or electrode, and the development of fuel cells [10–13]. Their high potential for the adsorptive removal of water pollutants relies on the well-developed pore structure, high specific surface area, chemical and thermal stability, and abundant functional groups, i.e., graphitic structures, C=O, C–O–C, –OH, and $–NH_2$ [9,12]. Moreover, the properties can be modified via chemical and physical methods to achieve target pollutants with high adsorption capacity, which can be used extensively in water treatment [12,14].

Some of them have been studied for the adsorption of OTC organic contaminants such as multi-walled carbon nanotubes [15], graphene oxide [16], activated carbon [9,17], biochar [18,19], and biological sludge [20]. Their advantages include low cost, the abundance of raw materials, chemical stability, and high surface area, which is mainly attributed to the presence of micropores and mesopores [21].

However, conventional carbon-based adsorbents have irregular and defective pore structures with limited interconnectivity, which inhibits mass transfer and diffusion, thus restricting molecular access to the adsorbent surfaces [22–24]. In this regard, hierarchically porous carbon (HPC) can be an efficient alternative to conventional carbon-based materials. HPC is characterized by a well-defined pore structure consisting of both micropores and mesopores, with a pore size distribution that spans a range of less than 2 nm to 50 nm [25,26].

HPCs are generally prepared using templates, such as nanoscale spheres of SiO_2, resorcinol formaldehyde resin, and $CaCO_3$ [25,27]. The use of templates results in complex synthesis procedures and the generation of acidic wastewater. On the other hand, the drawbacks can be ruled out using the activation of pyrolysis, which is one of the template-free methods. In general, chemical activation can partially oxidize/gasify the components of carbon-based materials, which leads to a significant increase in the number of micropores and mesopores and the transformation of surface functional groups [28,29].

The relative abundance of micropores and mesopores in HPC generated by chemical activation depends on several factors, including the sources of the material and the activation conditions, such as the type of activating agent, its concentration, temperature, and time [23]. For example, insufficient and excess use of an activation agent results in poor and amorphous pore structures and pore coalescence or collapse, respectively [30,31]. The creation of pores and increased surface area are promoted with increasing temperature, but it is accompanied by the destruction of micropores, increases in fixed carbon and ash content, and the excessive volatilization of functional groups [23,31]. Therefore, the establishment of activation conditions is essential to the development of required pore structures. However, it also suggests that the pore structures in HPCs can be controlled by the activation conditions, which increases the variety of potential applications of HPCs.

Other than the activation conditions, the selection of a carbonaceous raw material is also very important when aiming to prepare an HPC of a specific purpose, such as an adsorbent or a supercapacitor [25,32]. It was reported that the pores and microscopic structures of carbonized biomasses, i.e., biochars, are greatly influenced by feedstock structures, as demonstrated by the biochars derived from rice straw, swine manure, Douglas fir (*Pseudotsuga menziessii*), and hybrid poplar (*Populous deltoids*) [33,34]. In general, the raw organic materials used as precursors of HPC need to satisfy a couple of requirements: first, they must be capable of producing a substantial amount of HPC following heat treatment, and second, they must be able to fabricate carbons with a disordered microstructure (non-graphitizable carbon). The carbon sources that meet both requirements are biomass-derived products and certain types of polymers [11,23,35].

Meanwhile, chemical activation involves the mixing of an activating agent, such as H_3PO_4, $ZnCl_2$, KOH, and $NaHCO_3$, with a raw material, followed by high-temperature treatment in an inert gas atmosphere [36,37]. The most widely used chemical activator is

KOH, but it has a critical drawback in that it is an extremely corrosive substance according to NFPA 704 hazard labels [35], limiting the use of it at an industrial level. Thus, the use of more benign activating agents (e.g., sodium bicarbonate ($NaHCO_3$)) that lead to a greener activation process is required [35,38].

Regarding the above, in this study, wheat flour (WF)-based HPC was fabricated with $NaHCO_3$ as the activator under various activation conditions. WF has been used in attempts to prepare supercapacitors [10,11]. However, the activation conditions must be optimized for the resultant material to have the optimum property for the adsorption of organic pollutants, such as OTC. For example, the adsorption is largely attributable to the defects, mesopores, and the degree of graphitization for a better transport and for the π–π electron–donor–acceptor (EDA) interactions [9,12], while the capacitance is more related to the micropores and O-containing groups [10,11]. Therefore, the HPCs were characterized using various techniques such as N_2 adsorption/desorption isotherms, scanning electron microscopy (SEM), X-ray diffraction (XRD), Fourier Transform Infrared (FTIR) spectroscopy, and Raman spectroscopy to analyze the pore structure and surface properties. The adsorption of OTC on to the HPCs were evaluated using the kinetics and equilibrium of OTC adsorption. In addition, the activation condition, characteristics, and the adsorption performance were discussed comprehensively.

2. Materials and Methods

2.1. Materials and Reagents

WF was purchased from Homeplus Co., Ltd. (Seoul, Republic of Korea). $NaHCO_3$ and ethanol (C_2H_5OH, ≥99.9%) were acquired from Samchun (Seoul, Republic of Korea). Oxytetracycline hydrochloride ($C_{22}H_{24}N_2O_9 \cdot HCl$, OTC·HCl), hydrochloric acid (HCl, 37%), and sodium hydrate (NaOH, ≥97%) were acquired from Merck KGaA (Darmstadt, Germany). The chemicals were all of analytical grade and utilized as they were received. The deionized water was obtained from the water purification system, Aquapuri 551 system (Younglin, Anyang, Republic of Korea).

2.2. Preparations of HPCs

HPC was prepared via the pyrolysis of WF and $NaHCO_3$ mixture according to previous work with some necessary modification [38]. Typically, 24 g of wheat powder was mixed with a different amount of $NaHCO_3$ (0 g, 12 g, 24 g) and poured into 300 mL of distilled water to produce a paste under stirring. Then, the paste was carbonized at different temperatures (600, 800, and 900 °C) with a 5 °C/min heating rate for a different activation time (1, 2, and 3 h) under N_2 atmosphere. The temperature was selected by considering previous studies, which state that an organic material is carbonized over 600 °C [39]. The resulting black powder was rinsed sequentially with diluted HCl solution (1 M), deionized water, and ethanol. It was dried for 12 h at 80 °C and then ground. The final product was named HPCX_RY_ZH, where X is the activation temperature, Y is the mass ratio between activator and biomass ($NaHCO_3$/WF, g/g), and Z is the activation time.

2.3. Materials Characterization

The pore structure and the specific surface area were analyzed using a BELSORP-mini (Microtrac BEL, Osaka, Japan). The N_2 adsorption/desorption isotherms of the HPCs were obtained at 77K after degassing at 110 °C for 2 h under N_2 gas. The Brunauer–Emmett–Teller (BET) method was used to calculate the specific surface area (SSA), and the total pore volume (PV) was evaluated at a relative pressure (P/P_o) of 0.99. The *t*-plot method was used to estimate micropore volume. The HPCs were sputtered with Pt, and the microscopic images were taken using a field emission SEM (FE-SEM; Carl Zeiss, Oberkochen, Germany). Raman spectra were obtained using an in Via Raman microspectrometer (Renishaw, Wotton-under-Edge, UK) with a 514 nm excitation wavelength and 4 cm^{-1} spectral resolution. FTIR spectra were listed at 4000–400 cm^{-1} with the pellets prepared from the mixture of 0.2 mg HPC and 200 mg of KBr, using an FTIR spectrophotometer (Spectrum One System,

Perkin-Elmer, Waltham, MA, USA). XRD patterns were obtained using a DB Advance X-ray diffractometer (Bruker, MA, USA) in the 2θ range of 5–69.9925°. The zeta potential was analyzed in the pH range of 2–11 using a zeta potential analyzer (ZetaPlus, Brookhaven Instruments, New York, NY, USA), and with a suspension of 5 g/L HPCs in a 0.01M KCl aqueous solution.

2.4. Adsorption Experiments

Batch adsorption kinetic experiments were conducted in a 250 mL amber bottle with continuous mixing. The HPCs were dispersed in DIW, followed by the introduction of OTC stock solution. Samples were taken at predetermined times. The equilibrium adsorption isotherm experiments were performed in 50 mL amber glass tubes. The 0.025 g of the HPCs were dispersed in 40 mL OTC solution of 10–600 mg/L. The tubes were shaken in a shaking water bath (BS-31, Lab Companion, JEIO Tech., Daejeon, Republic of Korea) for 4 h at 298, 308, and 318 °K. All samples were filtered through a 0.45 μm polyvinylidene fluoride (PVDF) filter, and then the concentration of OTC in the filtrates was measured by a UV–visible spectrophotometer (UV-1280, Shimadzu, Kyoto, Japan) at 358 nm. All experiments were conducted in triplicate. The pH did not change during the experiments and was 5.60 ± 0.25 for all experiments, unless noted otherwise.

2.5. Modeling of Adsorption

The results of adsorption kinetic experiments were fitted to a pseudo-first-order adsorption kinetic model (Equation (1)), a pseudo-second-order adsorption kinetic model (Equation (2)), an intra-particle diffusion model (Equation (3)), and an Elovich equation (Equation (4)):

$$\frac{dq_t}{dt} = k_{a1}(q_e - q_t), \tag{1}$$

$$\frac{dq_t}{dt} = k_{a2}(q_e - q_t)^2, \tag{2}$$

$$q_t = k_{id}(t)^a, \tag{3}$$

$$\frac{dq_t}{dt} = \alpha_{El} exp(-\beta_{El} q_t), \tag{4}$$

where, q_t is the amount of OTC adsorbed at time t (min) (mg/g), q_e is the equilibrium adsorption amount (mg/g), k_{a1} is the pseudo-first-order adsorption rate constant (min^{-1}), k_{a2} is the pseudo-second-order adsorption rate constant (g/mg·min), k_{id} is the rate constant of intra-particle diffusion, α_{El} is the initial adsorption rate (mg/g·min), and β_{El} is a constant related to the surface coverage and activation energy of adsorption (g/mg). The experimental results were fitted to the models via nonlinear fitting, using MATLAB (R2021a, The MathWork, Inc., Natick, MA, USA).

The results of the equilibrium adsorption isotherm experiments were described using Langmuir (Equation (5)), Freundlich (Equation (6)), and Temkin (Equation (7)) isotherms:

$$q_e = q\frac{K_L C_e}{1 + K_L C_e}_{max}, \tag{5}$$

$$q_e = K_F {C_e}^{1/n}, \tag{6}$$

$$q_e = \frac{RT}{b_T} ln(A_T C_e), \tag{7}$$

where, q_e is the equilibrium adsorption amount (mg/g), q_{max} is the maximum adsorption capacity (mg/g), C_e is the equilibrium concentration of OTC (mg/L), K_L is the Langmuir adsorption constant (L/mg), K_F is the Freundlich constant ((mg/g)·$(L/mg)^{1/n}$), $1/n$ is a

constant related to the adsorption intensity, R is the gas constant (8.314 J/mol·°K), T is the absolute temperature (K), b_T is the Temkin constant associated with the heat of adsorption (J/mol), and A_T is the Temkin equilibrium constant (L/mg).

3. Results and Discussion

3.1. Characterization of HPCs

3.1.1. Microstructure and Pore Structure

The FE-SEM images of all HPCs showed the co-existence of macropores, mesopores, and micropores, indicating that the hierarchical porous structures have been successfully fabricated (Figure 1). The carbonization of WF activated by $NaHCO_3$ led to form a 3D scaffolding framework [38]. The surfaces of HPC900_R0.5_2H (Figure 1B) were rougher and more aggregates of smaller particles were found, suggesting more developed pore structures than those of HPC600_R0.5_2H (Figure 1A). The effects of $NaHCO_3$ dose are shown in Figure 1B–D for the ratio of $NaHCO_3$ to WF of 0, 0.5, and 1.0, respectively. The HPC900_R0.0_2H showed a negligible development of surface pores. However, surface pores increased as the activator dose increased, because of the increase in the release of gaseous products and the expansion of the graphitic lattices via the intercalates generated by the metallic Na [40]. The effects of activation time are shown in Figure 1B,E,F, showing the surfaces of the HPCs activated for 1, 2, and 3 h, respectively. The surface of HPC900_R0.5_1H displayed macropores on its surface, and they increased with increasing activation time (HPC900_R0.5_2H and HPC900_R0.5_3H). In addition, small pores were found on the surface of HPC900_R0.5_3H, which can be assigned to the exposed mesopores (the inset of 1(F)).

These clearly suggest the detrimental effects of $NaHCO_3$ dose, temperature, and activation time on the pore structure of HPCs, which led to the enhanced hierarchical pore structure in the carbonized WF, as they increased, under the conditions in this study [30,35,38]. However, the inner-sphere pores could not be properly characterized by the images in Figure 1. Therefore, the details of the effects of the activation conditions on the pore structures were further investigated with specific surface area (SSA), total pore volume (V_{total}), mesopore volume (V_{meso}), micropore volume (V_{micro}), and average pore diameter (d_a) of the HPCs (Tables 1–3), using N_2 adsorption/desorption isotherms.

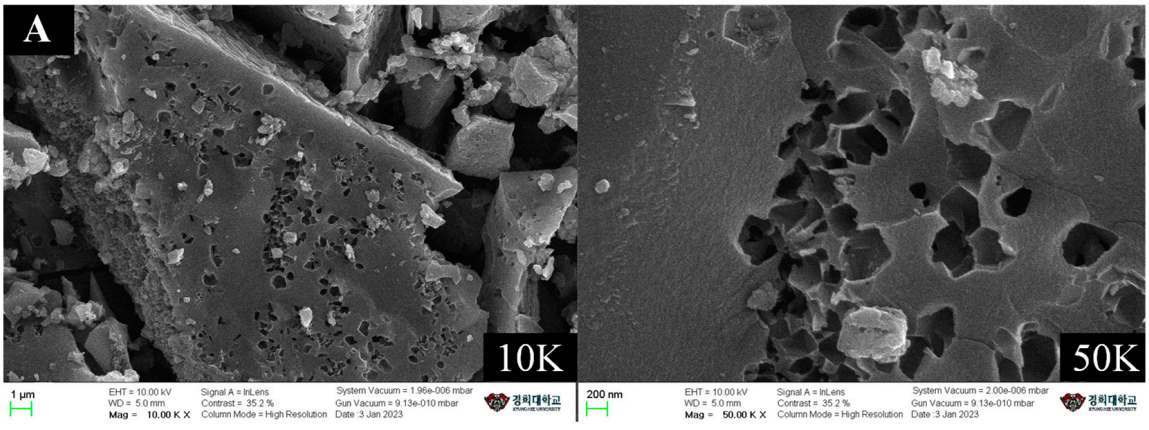

Figure 1. *Cont.*

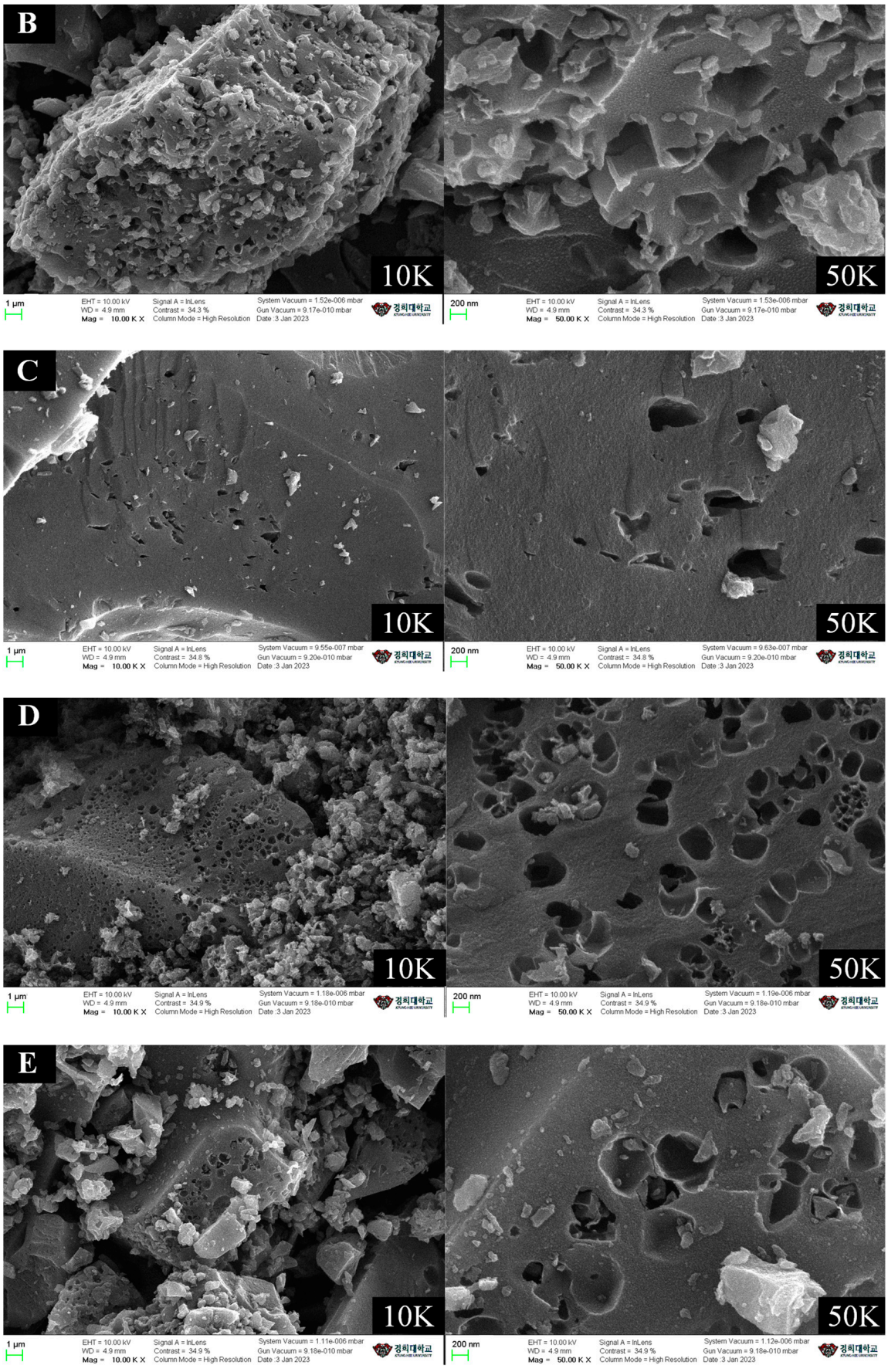

Figure 1. *Cont.*

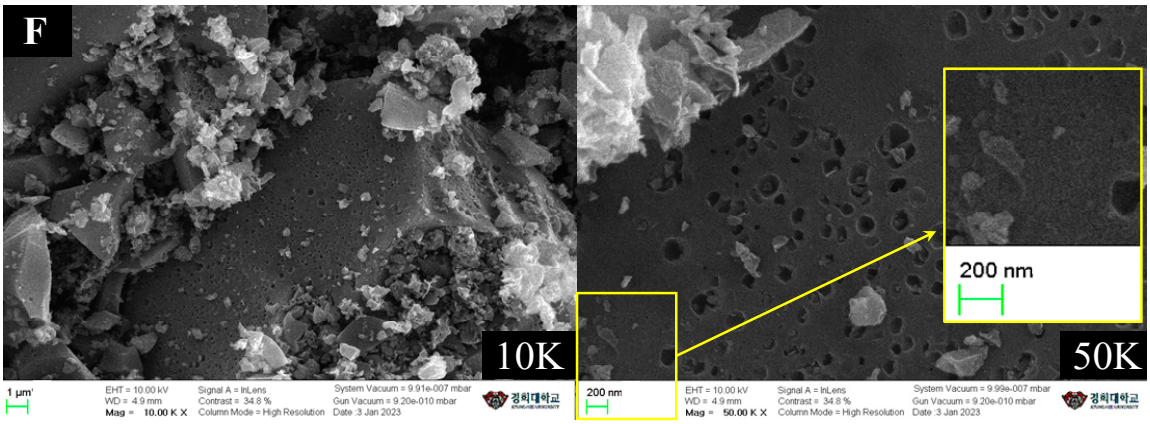

Figure 1. SEM images of the (**A**) HPC600_R0.5_2H, (**B**) HPC900_R0.5_2H, (**C**) HPC900_R0.0_2H, (**D**) HPC900_R1.0_2H, (**E**) HPC900_R0.5_1H, and (**F**) HPC900_R0.5_3H.

Table 1. Pore characteristics of HPCs as a function of pyrolysis temperature.

	Specific Surface Area (SSA) (m^2/g)	Total Pore Volume (V_{total}) (cm^3/g)	Micropore Volume (V_{micro}) (cm^3/g)	Mesopore Volume (V_{meso}) (cm^3/g)	V_{meso}/V_{total}	Average Pore Diameter (d_a) (nm)
HPC600_R0.5_2H	460.54	0.2281	0.1779	0.0366	0.1605	1.9811
HPC800_R0.5_2H	622.29	0.2879	0.2513	0.0369	0.1282	1.8505
HPC900_R0.5_2H	648.13	0.2908	0.2539	0.0502	0.1726	1.7947

Table 2. Pore characteristics of HPCs as a function of the ratio between WF and $NaHCO_3$.

	Specific Surface Area (SSA) (m^2/g)	Total Pore Volume (V_{total}) (cm^3/g)	Micropore Volume (V_{micro}) (cm^3/g)	Mesopore Volume (V_{meso}) (cm^3/g)	V_{meso}/V_{total}	Average Pore Diameter (d_a) (nm)
HPC900_R0.0_2H	662.75	0.2750	0.2611	0.0139	0.0505	1.6595
HPC900_R0.5_2H	648.13	0.2908	0.2539	0.0369	0.1269	1.7947
HPC900_R1.0_2H	633.30	0.4382	0.3070	0.1312	0.2994	2.7678

Table 3. Pore characteristics of HPCs as a function of activation time.

	Specific Surface Area (SSA) (m^2/g)	Total Pore Volume (V_{total}) (cm^3/g)	Micropore Volume (V_{micro}) (cm^3/g)	Mesopore Volume (V_{meso}) (cm^3/g)	V_{meso}/V_{total}	Average Pore Diameter (d_a) (nm)
HPC900_R0.5_1H	259.01	0.1169	0.0975	0.0194	0.1659	1.8054
HPC900_R0.5_2H	648.13	0.2908	0.2539	0.0369	0.1269	1.7947
HPC900_R0.5_3H	720.81	0.3720	0.3044	0.0676	0.1817	2.0643

The *SSA* and V_{total} of the HPCs increased greatly as the pyrolysis temperature was elevated from 600 °C to 800 °C, but slightly when it was further raised to 900 °C. Table 1 shows that the increased *SSA* and V_{total} were attributed to the formation and decrease in micropores and mesopores, respectively, resulting in the decrease in d_a. It was reported that Na_2CO_3 and the C in biomass are thermally decomposed to form Na_2CO_3, H_2O, CO, and CO_2 (Equations (8) and (9)), under relatively low temperatures [38]. An increase in temperature near to or over the fusion point of Na_2CO_3, i.e., 851 °C, Na_2CO_3 and its byproduct (NaO) are decomposed to Na and CO, generating micropores [23,38]. In

addition, mesopores of carbonaceous materials would be broken into smaller pores under high temperature [30,38].

$$2NaHCO_3 \rightarrow Na_2CO_3 + CO_2 + H_2O, \quad (8)$$

$$C + CO_2 \rightarrow 2CO, \quad (9)$$

$$Na_2CO_3 \rightarrow Na_2O + CO_2, \quad (10)$$

$$Na_2CO_3 + 2C \rightarrow 2Na + 3CO, \quad (11)$$

$$Na_2O + C \rightarrow 2Na + CO, \quad (12)$$

Table 2 shows that the *SSA* slightly decreased, while the V_{total} significantly increased as the ratio of $NaHCO_3$ to WF increased from 0 (no activator) to 1.0. It is thought that the increase in V_{total} is largely attributed to the increase in mesopores, considering the slight and great increase in V_{micro} and V_{meso}, respectively (Table 2). This indicates that the release of CO, CO_2, and H_2O (Equations (8)–(12)) results in the formation of mesopores, rather than micropores, as well as in the widening of existing micropores via their destruction [30,31,41]. On the other hand, the *SSA* was the highest when no $NaHCO_3$ was added, i.e., HPC900_R0.0_2H, and the decrease in the *SSA* was not as significant as the increase in the *SSA* with increasing temperature (Table 1). Table 3 shows that the *SSA*, V_{total}, and V_{micro} greatly increased when the activation time increased from 1 to 2 h, but less significantly with a further increase to 3 h. The V_{micro} showed a linear correlation with the activation time (Pearson correlation coefficient of 0.988).

Considering the results presented in Tables 1–3, it is suggested that the *SSA* and V_{micro} in the HPCs are more dependent on the activation time rather than temperature and $NaHCO_3$ dose, while V_{meso} is the most significantly affected by $NaHCO_3$ dose. However, the dominance of micropores was found for all HPCs, ranging from 70.1 (HPC900_R1.0_2H) to 95.0 (HPC900_R0.0_2H) %. The plot of adsorption–desorption isotherm and the pore size distribution can be found on Figures S1 and S2, respectively.

3.1.2. FTIR Spectroscopy

Figure 2 displays the FTIR spectra of the HPCs, showing the common bands, corresponding to –OH stretching (at 3430 cm^{-1}), aliphatic C-H_n stretching (at 2920 and 2850 cm^{-1}), adsorbed CO_2 (at 2360 and 2335 cm^{-1}), and aromatic C=C and/or conjugated C=O stretching (at 1630 cm^{-1}) [30,42].

The intensities of the –OH and CO_2 bands decreased, while those of the bands of aliphatic C–H_n and C=C/C=O did not exhibit any notable changes, as the temperature increased from 600 to 900 °C (Figure 2A). This indicates that more –OH and CO_2 was decomposed and/or volatilized over 600 °C, while the aliphatic C–H_n and C=C/C=O were formed at 600 °C and are thermally stable at the temperature up to 900 °C [31,43].

The intensities of the –OH, C–H_n, and CO_2 bands decreased with increasing $NaHCO_3$ amount (Figure 2B). The band of C=C/C=O decreased, and the noise of the band also decreased, as the ratio increased from 0 to 0.5, indicating the formation of more rigid structures with a higher degree of graphitization when an activator ($NaHCO_3$) was used [43]. An increase in the injection counts of the $NaHCO_3$ (HPC900_R1.0_2H) resulted in increased intensity and noises of the C=C/C=O band, suggesting more amorphous aromatic structures.

The intensity of the CO_2 band decreased with increasing activation time, while that of –OH, C–H_n, and C=C/C=O decreased and then increased, as the time increased from 1, 2, and then 3 h (Figure 3C). This indicates an increase in the abundance of the functional groups on the HPC surfaces via intermolecular interactions under a longer reaction time [44]. This is also attributable to the etching effect of $NaHCO_3$ on the porous carbon during a longer activation process [31].

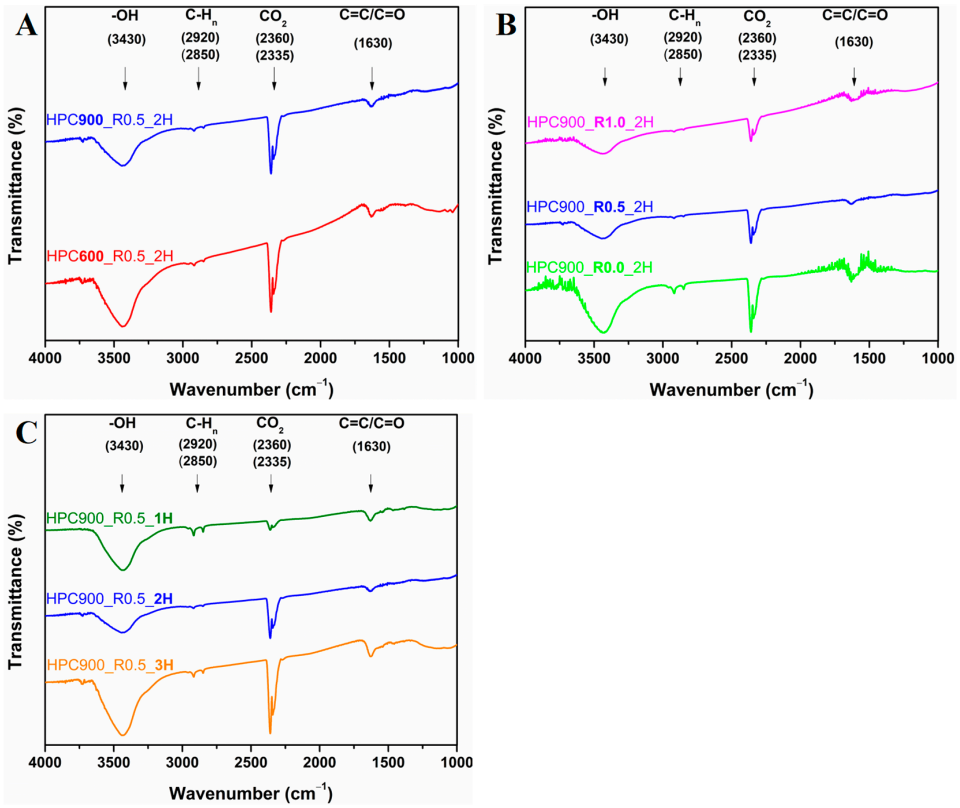

Figure 2. FTIR spectra of HPCs by (**A**) temperature effect, (**B**) ratio effect, (**C**) activation time effect.

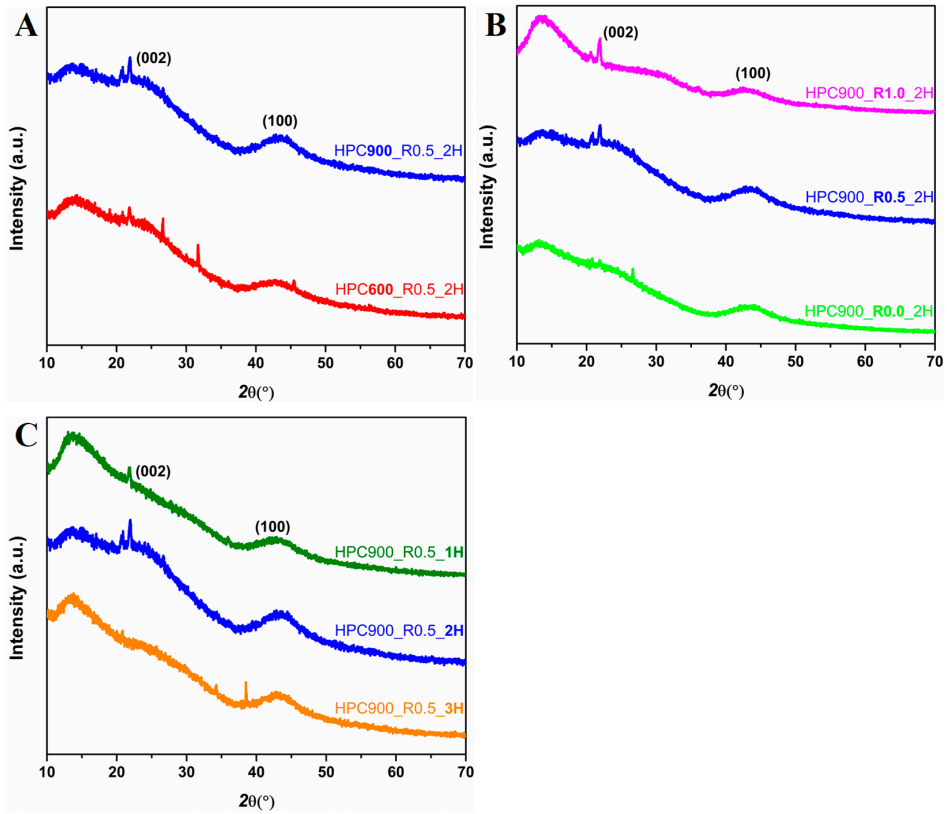

Figure 3. XRD patterns of HPCs by (**A**) temperature effect, (**B**) ratio effect, (**C**) activation time effect.

3.1.3. XRD

The XRD patterns of all of the HPCs exhibit two peaks at the 2θ of ~24° and ~44°, which correspond to the (002) plane of the interlayer spacing and (100) planes of the graphitic structures, respectively, as demonstrated in the literature (Figure S3) [11,38]. Also, a sharp peak at 2θ of ~14°, which corresponds to the signal of the native starch from wheat flour, was found [45,46].

Figure 3A displays that the XRD spectra of HPC600_R0.5_2H showed some small peaks at 2θ of ~23°, ~27°, and ~33°, indicating the presence of Na_2CO_3 formed from $NaHCO_3$ decomposition (Equation (8)) [38]. For HPC900_R0.5_2H, the peaks of (002) and (100) planes were more intense and wider than those in HPC600_R0.5_2H, and the peaks of Na_2CO_3 disappeared and were replaced by two (2) peaks near ~22°, which may correspond to the decomposition of Na_2CO_3 to Na_2O (Equation (9)). These changes in the XRD patterns by increasing the temperature condition suggest an increase in the degree of graphitization, due to the existence of more pores and defects in carbon material [10,38,44].

Figure 3B shows that the XRD pattern of the HPC prepared without $NaHCO_3$ (HPC900_R0.0_2H) consists of (002) and (100) planes of graphitic structures, as well as a peak of starch, but no notable peaks of Na_2CO_3 (2θ of ~23°, ~27°, and ~33°) or Na_2O (2θ of ~22°). The peaks of (002) and (100) planes became more intensive and sharp peaks of Na_2O were detected as the amount of $NaHCO_3$ increased, i.e., HPC900_R0.5_2H, demonstrating the activator's evident impact on the formation of more crystalline graphitic structures. On the other hand, the pattern of HPC900_R1.0_2H shows that the intensity of the peaks of (002) and (100) planes was depleted, while that of the peak at 2θ of ~22° became stronger. This suggests that this could be explained due to the abundant availability of Na_2O (Equations (8) and (9)), leading to an increase in the formation of pores and defects, but resulting in a decreased degree of graphitization and crystallinity [38].

The XRD pattern of the HPC, prepared at 900 °C and 1 h, consists of the peaks of (002) and (100) planes, as well as of Na_2CO_3 (Figure 3C). An additional peak of Na_2O was found in that of HPC900_R0.5_2H, and the intensities of the peaks of (002) and (100) planes increased, indicating more developed graphitic structures. However, with the additional one hour of activation time, i.e., HPC900_R0.5_3H, the peaks of Na_2CO_3 and Na_2O disappeared and the (002) plane weakened, indicating the complete decomposition of $NaHCO_3$, Na_2CO_3, and Na_2O, which can lead to more pores created as well as more defects. It has been reported that a longer thermal treatment under a higher temperature is responsible for the depletion of certain minerals, such as Na_2O and quartz [44,47].

3.1.4. Raman Spectroscopy

The Raman spectra of HPCs are illustrated in Figure 4A, and they were deconvoluted into seven (7) bands, as illustrated in Figure 4B for HPC900_R0.5_3H. The bands were at 1210, 1350–1351, 1540–1541, 1580–1581, 1610, 2900–2923, and 2626–2670 cm^{-1}, which are assigned to D4, D, D3 (D′), G, D2 (D′), 2D (G′), and 2D+G (D+D′) bands, respectively.

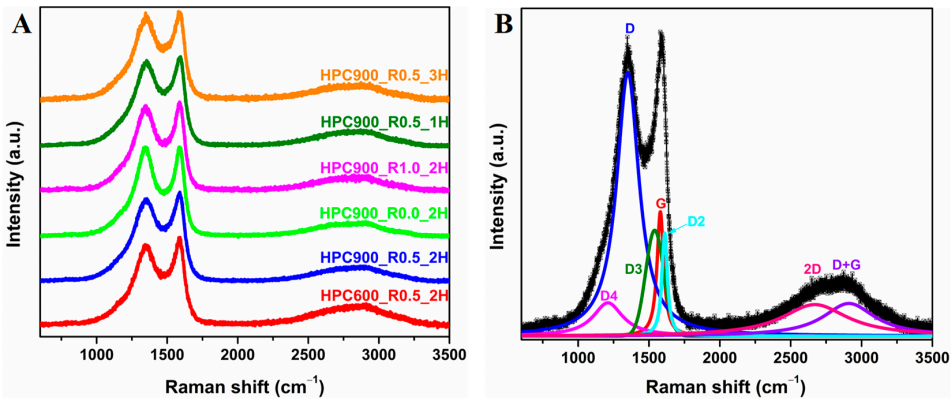

Figure 4. (**A**) Raman spectra of HPCs and (**B**) deconvolution Raman spectra of HPC900_R0.5_3H.

The D4 band is associated with disordered graphitic lattice, polyenes, and ionic impurities. The bands of D, D3 (D′), G, and D2 (D′) are associated with disordered graphitic lattice induced by the sp^3 hybridization such as graphene layer edges, amorphous carbon, ideal graphitic lattice, and disordered graphitic lattice in surface graphene layers, respectively. The intensity of the D band was substantial for all HPCs, suggesting that all of them possess a high degree of defects and porosity [48]. The 2D and D+G bands are associated with single-layer graphene and a combination of the D and G bands, respectively [49]. Therefore, the ratio of the area of D band to G band (I_D/I_G) can be used to evaluate the degree of structural defects and disorder, as well as the sizes of the graphite nanocrystallites, in carbon materials OTC [50]. The ratio of 2D and to G band (I_{2D}/I_G) is an indicator of the relative abundance of single-layer graphene in a graphitic structure, while the types of the defects can be suggested by that of D band to D2 band (I_D/I_{D2}).

Table 4 shows that the I_D/I_G increased from 4.528 to 7.887 as the temperature increased from 600 °C (HPC600_R0.5_2H) to 900 °C (HPC900_R0.5_2H). This points out the increase in disordered carbon structures or defects in the HPCs, while the size of the carbon crystallites decreased, with increasing temperature [10,38,48]. These suggest a higher capacity of surface chemical reactions and adsorption via accelerated electron transfer and stronger π–π interactions [50,51] for HPC900_R0.5_2H than for HPC600_R0.5_2H. The I_{2D}/I_G also increased from 1.579 (HPC600_R0.5_2H) to 1.776 (HPC900_R0.5_2H), which agrees with the increase in I_D/I_G. On the other hand, the I_D/I_{2D} decreased from 15.700 to 11.883 for HPC600_R0.5_2H and HPC900_R0.5_2H, respectively. This indicates that the defects in HPC600_R0.5_2H and HPC900_R0.5_2H were more associated with sp^3–C-related defects and hopping defects, respectively [41].

Table 4. Result of Raman spectroscopy of HPCs with different activation temperatures.

		D4	D	D3	G	D2	D+G	2D	I_D/I_G	I_{2D}/I_G	I_D/I_{D2}
HPC600_	Center (cm^{-1})	1210	1350	1540	1580	1610	2900	2660	4.528	1.579	15.700
R0.5_2H	Fraction (%)	0.126	0.584	0.124	0.129	0.037	0.599	0.401			
HPC900_	Center (cm^{-1})	1210	1350	1541	1580	1610	2906	2670	7.887	1.766	11.883
R0.5_2H	Fraction (%)	0.097	0.637	0.131	0.081	0.054	0.567	0.433			

The I_D/I_G and I_{2D}/I_G increased from 4.821 to 7.959 and from 1.638 to 2.818, respectively, while the I_D/I_{2D} decreased from 12.607 to 10.765, as the $NaHCO_3$ amount increased (Table 5). In addition, the results in Table 6 show an increase in the I_D/I_G and I_{2D}/I_G, from 5.729 to 7.888 and from 1.603 to 1.953, respectively, and a decrease in the I_D/I_{2D}, from 19.451 to 9.746, with increasing activation time.

Table 5. Result of Raman spectroscopy of HPCs with different activator dose.

		D4	D	D3	G	D2	D+G	2D	I_D/I_G	I_{2D}/I_G	I_D/I_{D2}
HPC900_	Center (cm^{-1})	1210	1350	1540	1580	1610	2915	2670	4.821	1.638	12.607
R0.0_2H	Fraction (%)	0.114	0.592	0.124	0.123	0.047	0.410	0.590			
HPC900_	Center (cm^{-1})	1210	1350	1541	1580	1610	2906	2670	7.887	1.766	11.883
R0.5_2H	Fraction (%)	0.097	0.637	0.131	0.081	0.054	0.567	0.433			
HPC900_	Center (cm^{-1})	1210	1351	1540	1580	1610	2911	2670	7.959	2.818	10.765
R1.0_2H	Fraction (%)	0.105	0.625	0.133	0.079	0.058	0.448	0.552			

The results in Tables 4–6 strongly suggest that an increase in activator dose, elevating temperature, and a prolonged activation time commonly induced similar changes in the HPCs, such as increasing the degree of defects, especially hopping defects, and the relative number of single-layer graphenes. However, the most and the least significant factors for the I_D/I_G were temperature and activation time, respectively; for the I_{2D}/I_G, they were activator amount and temperature, respectively; and for the I_D/I_{2D}, they were activation

time and activator amount, respectively. Therefore, it is suggested that the degree of defects, formation of graphene layers, and the relative abundance of hopping defects are mostly governed by temperature, activator amount, and activation time, respectively.

Table 6. Result of Raman spectroscopy of HPCs with different activation time.

		D4	D	D3	G	D2	D+G	2D	I_D/I_G	I_{2D}/I_G	I_D/I_{D2}
HPC900_	Center (cm^{-1})	1210	1351	1541	1580	1610	2911	2670	5.729	1.603	19.451
R0.5_1H	Fraction (%)	0.107	0.621	0.132	0.108	0.032	0.493	0.507			
HPC900_	Center (cm^{-1})	1210	1350	1541	1580	1610	2906	2670	7.887	1.766	11.883
R0.5_2H	Fraction (%)	0.097	0.637	0.131	0.081	0.054	0.567	0.433			
HPC900_	Center (cm^{-1})	1210	1350	1540	1580	1610	2900	2660	7.888	1.953	9.764
R0.5_3H	Fraction (%)	0.088	0.647	0.117	0.082	0.066	0.542	0.458			

3.2. Adsorption of OTC

3.2.1. Effect of Activation Conditions of HPCs on OTC Adsorption Kinetics

The effects of the activation conditions on the OTC adsorption kinetics by the HPCs are presented in Figure 5 and Table 7. As presented in Figure 5A, HPC900_0.5R_2H exhibits the highest adsorption rate and capacity compared to HPC600_0.5R_2H and HPC800_0.5R_2H. The pseudo-second-order kinetic model fits better for HPC600_0.5R_2H and HPC800_0.5R_2H, demonstrating that the OTC adsorption onto them is mainly attributable to chemical mechanisms and that the adsorption was affected by the OTC amount on the surfaces [9,13,44]. Meanwhile, the HPC900_R0.5_2H condition is better fitted with the Elovich equation model ($r^2 > 0.99$), demonstrating that the OTC adsorption onto HPC900_R0.5_2H is the combination of bulk and surface diffusion, as well as the chemisorption, on energetically heterogeneous surfaces [9,52].

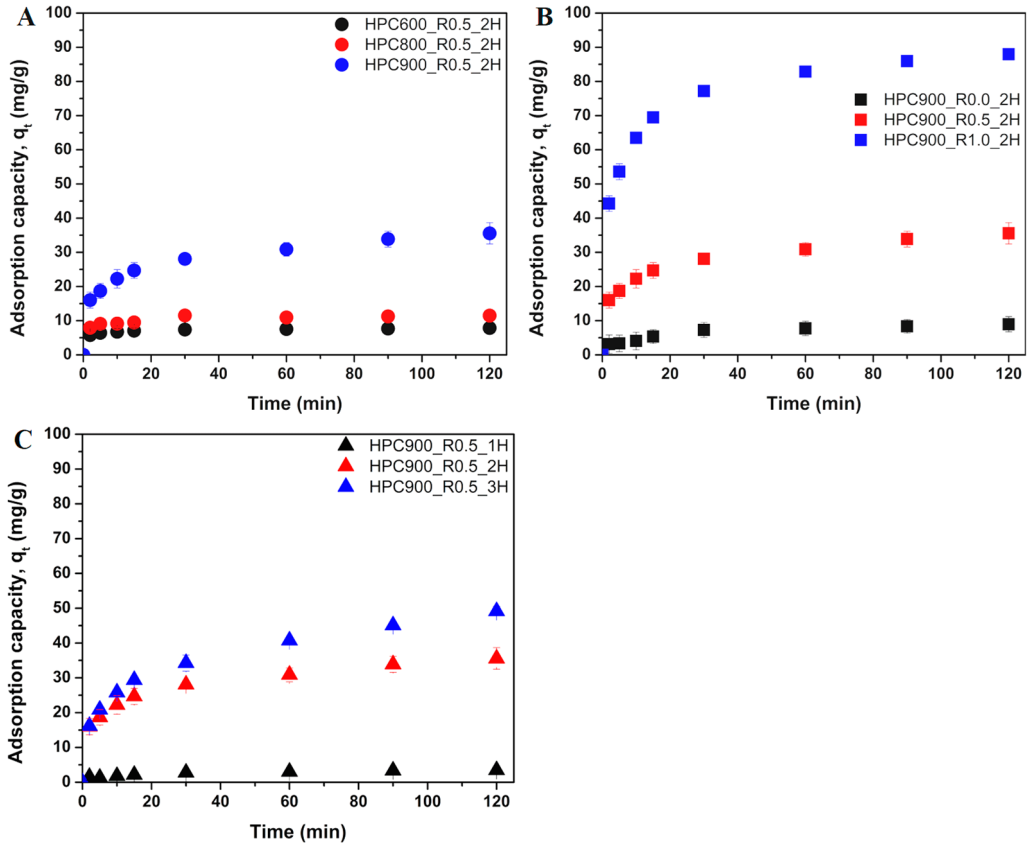

Figure 5. OTC adsorption kinetics by the HPCs prepared at different (**A**) temperature, (**B**) activator amount, and (**C**) activation time.

Table 7. Result of OTC adsorption kinetics using HPCs prepared with different temperatures, activator amount, and activation time.

Model		Temperature Effect			Activator Ratio Effect			Activation Time Effect		
		HPC600_ R0.5_2H	HPC800_ R0.5_2H	HPC900_ R0.5_2H	HPC900_ R0.0_2H	HPC900_ R0.5_2H	HPC900_ R1.0_2H	HPC900_ R0.5_1H	HPC900_ R0.5_2H	HPC900_ R0.5_3H
Pseudo-first-order	k_{a1} (min^{-1})	0.7164	0.0603	0.1746	0.0789	0.1746	0.2472	0.0938	0.1746	0.0981
	q_{e1} (mg/g)	7.3002	10.5649	31.0715	7.9271	31.0715	79.9331	3.1866	31.0715	42.8964
	r^2	0.9715	0.9356	0.8836	0.9172	0.8836	0.9252	0.8746	0.8836	0.8985
	SSE	1.36	6.68	112.04	5.21	112.04	463.43	1.27	112.04	194.00
Pseudo-second-order	k_{a2} (g/mg·min)	0.1752	0.0898	0.0079	0.0120	0.0079	0.0044	0.0399	0.0079	0.0029
	q_{e2} (mg/g)	7.6021	11.1119	33.5996	9.1863	33.5996	85.8779	3.4861	33.5996	47.4636
	r^2	0.9930	0.9716	0.9545	0.9550	0.9545	0.9812	0.9234	0.9545	0.9551
	SSE	0.33	2.95	43.79	1.05	43.79	116.59	0.78	43.79	85.86
Elovich Equation	α_{El} (mg/g)	16,253.980	1600.437	32.7913	2.5162	32.7913	202.7550	1.4056	32.7913	35.1593
	β_{El} (g/mg)	1.9062	1.0417	0.1878	0.5795	0.1879	0.0843	1.6265	0.1879	0.1135
	r^2	0.9575	0.8793	0.9964	0.9595	0.9964	0.9805	0.9433	0.9964	0.9929
	SSE	1.36	6.68	111.98	5.21	111.98	463.53	1.27	111.98	194.00

Note: SSE: Sum-Squared Error.

Figure 5B presents that OTC adsorption was greatly enhanced as the $NaHCO_3$ amount increased. It should be noted that HPC900_R0.0_2H showed the lowest OTC adsorption, even though it has the highest SSA (662.75 m^2/g). This could be explained by the poor development in mesopores and a higher fraction of micropores (Table 2), where the OTC diffusion is limited [23]. The adsorption was enhanced as the activation time increased (Figure 5C). It seems reasonable that this is attributable to the increased SSA and mesopores as given in Table 3.

Meanwhile, the Elovich equation model provided good fits to the OTC adsorption onto the HPCs prepared at 900 °C (HPC900_0.0R_2H, HPC900_0.5R_2H, HPC900_1.0R_2H, HPC900_0.5R_1H, and HPC900_0.5R_3H), regardless of activator amount and activation time. This strongly suggests that the temperature influenced the adsorption mechanisms more than the amount of activator or activation time. It was also supported by the more significant effect of the temperature on SSA and I_D/I_G, than activator amount and activation time (Tables 1–6). However, the performance, i.e., equilibrium adsorption amount and adsorption rate, was more significantly affected by the activator amount (Figure 5), by which the V_{meso} was the most influenced (Tables 1–3).

The OTC adsorption was further studied hereinafter, using HPC900_R1.0_2H, which showed the best performance.

3.2.2. Effect of pH

Figure 6A shows that the OTC removal was not notably affected in a pH range of 2–8, but significantly decreased as the pH further increased to 11. The pH would significantly affect adsorption, when it is largely governed by electrostatic interactions, influencing the charge of an adsorbent and an adsorbate. In particular, OTC has three (3) pK_as because of its multiple ionizable functional groups, making it an amphoteric molecule [53]. OTC dominantly exits as OTC^+ at pH < 3.4, OTC^0 at 3.4 < pH < 7.6, OTC^- at 7.6 < pH < 9.7, and OTC^{2-} at pH > 9.7 [54]. On the other hand, the pH_{PZC} of HPC900_R1.0_2H was 3.9, making the adsorbent renders positively and negatively charged, when the solution pH is under and over the pH_{PZC}, respectively (Figure 6B). However, the result in Figure 6A suggests that the OTC adsorption onto HPC900_R1.0_2H was not solely affected by the electrostatic interactions, but also significantly influenced by π–π EDA interactions and hydrophobic effects [55,56].

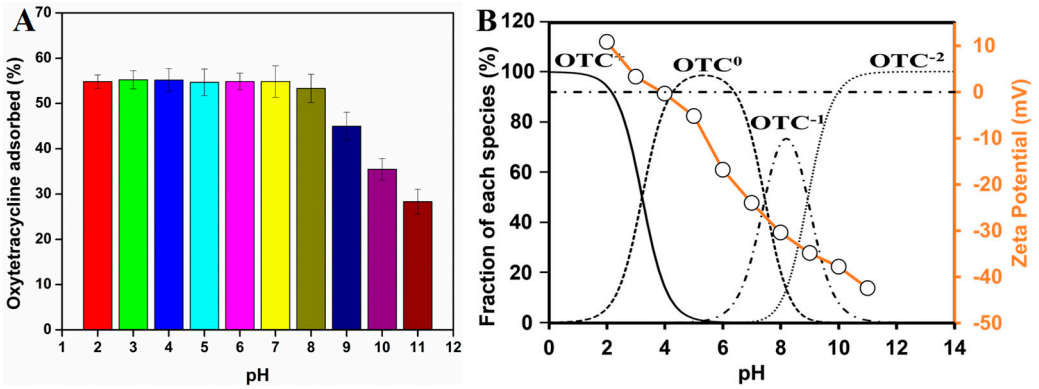

Figure 6. (**A**) The influence of pH on OTC adsorption on HPC900_R1.0_2H and (**B**) the zeta potential of HPC900_R1.0_2H with the speciation of OTC (Conde-Cid, 2020 [54]) (HPC900_R1.0_2H 0.1 g/L, OTC 10 mg/L).

As the pH is decreased, the π–electron-accepting ability of OTC increases; however, electrostatic repulsion increases because both HPC900_R1.0_2H and OTC are positively charged, and hydrophobicity decreases by protonation [13,56]. Under the pH 3.4 < pH < 7.6, OTC is apparently not charged, having the highest hydrophobicity. Therefore, the stable OTC adsorption at acidic-to-neutral pHs is attributable to the strong π–π EDA interactions, overwhelming the others, between OTC molecules, which accept π–electrons via the conjugated ionic structures, and the surfaces of HPC900_R1.0_2H, which donate π–electrons because of the C=O group and well-crystallized graphitic C–C [57]. On the other hand, the electrostatic repulsion increases because of the dominance of OTC^{-}/OTC^{2-} and the increase in negative charge on HPC900_R1.0_2H as the pH increased. In addition, the π–π EDA interactions are suppressed, and the hydrophobicity decreases because of deprotonation and ionization under alkaline conditions [26,56].

3.3. Adsorption Isotherm and Thermodynamic Study

The equilibrium adsorption amount (q_e) of OTC on HPC900_R1.0_2H gradually increased as the temperature increased from 298 to 318 °K (Figure 7). The three (3) widely used isotherm models (Langmuir, Freundlich, and Temkin) were selected to analyze the results [44,58]. Langmuir isotherm provided the best fit (Table 8), suggesting that the adsorption is homogeneous and monolayer, where the surface coverage does not influence the adsorption enthalpy [58]. The comparison of the OTC adsorption performance of different adsorbents can be found in Table S1. The HPC material has a higher adsorption capacity than most conventional biochars.

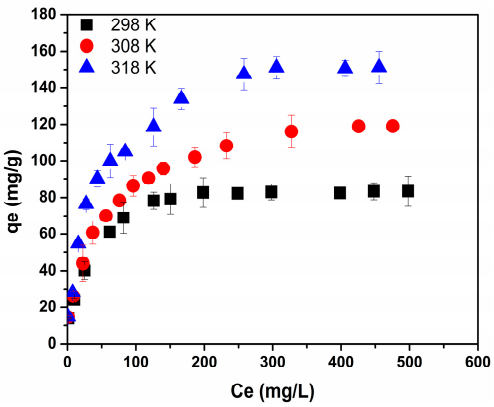

Figure 7. The adsorption isotherms of OTC on HPC900_R1.0_2H at different reaction temperatures.

Table 8. Result of adsorption isotherm.

Isotherm			**298 °K**	**308 °K**	**318 °K**
Langmuir	q_{max}	(mg/g)	87.184	128.370	162.707
	K_L	(L/g)	0.052	0.025	0.030
	r^2		0.999	0.995	0.996
	SSE		67.38	110.44	303.40
Freundlich	K_F	((mg/g)·(L/g)$^{1/n}$)	13.596	14.912	17.194
	n		3.082	2.763	2.571
	r^2		0.936	0.973	0.953
	SSE		901.64	683.14	1609.76
Temkin	b_T	(J/mol)	0.006	0.008	0.010
	A_T	(L/mg)	1.274	0.883	0.877
	r^2		0.936	0.939	0.951
	SSE		380.57	69.22	231.37

Equations (13) and (14) were used to calculate the Gibbs free energy change (ΔG^0) and the changes of enthalpy (ΔH^0) and entropy (ΔS^0) of the adsorption [9,59,60]:

$$\Delta G^0 = -RT \ln\left(K^0\right), \tag{13}$$

$$\ln\left(K^0\right) = -\frac{\Delta H^0}{RT} + \frac{\Delta S^0}{R} \tag{14}$$

where, K^0 is the equilibrium constant, calculated with the correlation of the OTC mass on the surface of the adsorbent (m_s) and that in the liquid phase (m_e), R is the ideal gas constant (8.314 J/mol·K), T is the absolute temperature (K), ΔG^0 is the standard Gibbs free energy change, ΔH^0 is the change in the standard Gibbs free energy change, and ΔS^0 is the change in the entropy. The correlation of ln (K^0) vs. 1/T can be found on Figure S4. Table 9 shows that ΔG^0 was negative and decreased with increasing temperature, implying that the adsorption is spontaneous. The ΔH^0 and ΔS^0 were positive, suggesting that the adsorption is endothermic and the increase in the randomness after adsorption, respectively. It is thought that the adsorption is dominated by chemisorption, considering that the ΔH^0 was over 40 kJ/mol [9,44,60,61].

Table 9. Thermodynamic parameters of OTC adsorption by HPC900_R1.0_2H.

		298 K	**308 K**	**318 K**
ΔG^0	(kJ/mol)	−3.093	−4.109	−6.028
ΔH^0	(kJ/mol)	40.788		
ΔS^0	(kJ/mol·°K)	0.147		

3.4. Discussion about the Stability and Regeneration

The stability of the HPCs for the adsorptive removal of organic pollutants, such as OTC, may not be important because adsorbents are generally wasted or regenerated after use due to the accumulated pollutants. However, the stability of catalysts is of high importance for the practical applications. The deactivation of catalysts at various degrees has been reported in a number of works found in the literature, for a biochar derived from wood shavings and thiourea–urea [62], Cu@Fe_3O_4 [63], GAC [64], Fe@NS-C-2-12 [65], nitrogen and phosphorus co-doped porous carbon [50], which are mainly attributable to the accumulation of the pollutants, and their byproducts, as well as the changes in the property of the catalysts.

The adsorption capacity of adsorbents generally decreases via the occupation of adsorption sites, the change of surface chemistry, and pore blockage [62,63,65]. It was reported that the adsorption capacity of DCF and VFX onto CS7 was decreased [25], while

the adsorption of OTC onto a poplar-leaf-derived biochar was decreased [66], as they were used repeatedly. However, the carbonaceous adsorbent can be successfully regenerated. The adsorption capacity of a biochar was recovered by pyrolysis at 800 °C for 2 h under nitrogen flow [66]. Thermal treatment can also improve the performance by increasing the extent of graphitization, which is advantageous for better structural stability and performance [9]. Therefore, it seems reasonable that carbonaceous adsorbents have a high potential of practical and economic applications.

4. Conclusions

In this study, $NaHCO_3$-activated WF-based HPCs were prepared under various conditions to investigate the conditions affecting their properties and OTC adsorption. It was demonstrated that the crystallinity of graphitic structures, degree of defects, the number of hopping defects, the stacking graphene-like layers, and pore structures were largely dependent on the activation conditions, while the functional groups were relatively less influenced by them. The activation temperature most significantly affected the adsorption mechanisms and the degree of defects, as evidenced by the increase in the I_D/I_G from 4.528 to 7.959, with increasing temperature from 600 to 900 °C, while the V_{meso} changed the most significantly from 0.1169 to 0.4382 cm^3/g, when the dose of the activator ($NaHCO_3$) increased from 0 to 100% of the WF mass. In addition, *SSA* increased greatly from 529.01 to 720.81 m^2/g, as the activation time increased from 1 to 3 h.

The best OTC adsorption capacity of 87.184–162.707 mg/g at 298–318 °K was achieved by the HPC prepared at 900 °C for 2 h, at the WF:$NaHCO_3$ ratio of 1:1 (w:w), i.e., HPC900_R1.0_2H, with the most abundant mesopores, suggesting the detrimental role of mesopores for the OTC adsorption onto HPCs.

The kinetics, equilibrium, and thermodynamics of OTC adsorption onto HPC900_1.0R_2H were good fits to the Elovich equation model and Langmuir isotherm, suggesting that the adsorption is the result of the combination of the diffusion and chemisorption, homogeneous, monolayer, spontaneous, and endothermic. No notable change in adsorption capacity was found under pH of 2–8, but it decreased substantially as the pH continued to increase, implying the crucial role of π–π EDA interactions and electrostatic attraction.

It is strongly suggested by the results in this study, that the HPCs derived from WF could be one of the excellent adsorbents for OTC removal, and that the performance of the HPCs can be controlled by the manipulation of the properties via changing activation conditions, which opens the opportunity of HPCs to a variety of applications.

Supplementary Materials: The following supporting information can be downloaded at: https://www.mdpi.com/article/10.3390/w15173146/s1, Figure S1: N_2 adsorption–desorption isotherms of HPCs by (A) temperature effect, (B) ratio effect, (C) activation time effect; Figure S2: Pore size distribution of HPCs by (A) temperature effect, (B) ratio effect, (C) activation time effect; Figure S3: XRD patterns of graphitic structure in (A) Yang et al. 2019 [1] and in (B) https://rruff.info/Graphite/R090047s (accessed on 6 August 2023); Figure S4: ln (K^0) vs. 1/T plot for HPC900_R1_2H; Table S1: Comparison of the maximum OTC adsorption performance of different adsorbents [65–71].

Author Contributions: Conceptualization and methodology, F.O.H.; validation and formal analysis, D.-G.K. and S.-O.K.; investigation, resources, data curation, and writing—original draft preparation, F.O.H.; writing—review and editing, D.-G.K. and S.-O.K.; visualization and supervision, S.-O.K.; project administration and funding acquisition, S.-O.K. All authors have read and agreed to the published version of the manuscript.

Funding: This work was supported by the National Research Foundation of Korea (NRF) grant funded by the Korean government (MSIT) (No. 2022R1A2B5B02001584).

Data Availability Statement: The data presented in this study are available upon request from the corresponding author.

Conflicts of Interest: The authors declare no conflict of interest.

References

1. Di Cerbo, A.; Palatucci, A.T.; Rubino, V.; Centenaro, S.; Giovazzino, A.; Fraccaroli, E.; Cortese, L.; Ruggiero, G.; Guidetti, G.; Canello, S.; et al. Toxicological Implications and Inflammatory Response in Human Lymphocytes Challenged with Oxytetracycline. *J. Biochem. Mol. Toxicol.* **2016**, *30*, 170–177. [CrossRef]
2. Li, D.; Yang, M.; Hu, J.; Ren, L.; Zhang, Y.; Li, K. Determination and fate of oxytetracycline and related compounds in oxytetracycline production wastewater and the receiving river. *Environ. Toxicol. Chem.* **2008**, *27*, 80–86. [CrossRef]
3. Cheng, X.; Guan, R.; Chen, Y.; Qian, Y.; Shang, Q.; Sun, Y. Adsorption and photocatalytic degradation process of oxytetracycline using mesoporous Fe-TiO2 based on high-resolution mass spectrometry. *Chem. Eng. J.* **2023**, *460*, 141618. [CrossRef]
4. Xu, L.; Zhang, H.; Xiong, P.; Zhu, Q.; Liao, C.; Jiang, G. Occurrence, fate, and risk assessment of typical tetracycline antibiotics in the aquatic environment: A review. *Sci. Total Environ.* **2021**, *753*, 141975. [CrossRef]
5. Li, Z.-J.; Qi, W.-N.; Feng, Y.; Liu, Y.-W.; Ebrahim, S.; Long, J. Degradation mechanisms of oxytetracycline in the environment. *J. Integr. Agric.* **2019**, *18*, 1953–1960. [CrossRef]
6. Pelosato, R.; Bolognino, I.; Fontana, F.; Sora, I.N. Applications of Heterogeneous Photocatalysis to the Degradation of Oxytetracycline in Water: A Review. *Molecules* **2022**, *27*, 2743. [CrossRef]
7. Wang, H.; Guo, W.; Liu, B.; Si, Q.; Luo, H.; Zhao, Q.; Ren, N. Sludge-derived biochar as efficient persulfate activators: Sulfurization-induced electronic structure modulation and disparate nonradical mechanisms. *Appl. Catal. B Environ.* **2020**, *279*, 119361. [CrossRef]
8. Xu, Y.; Liu, S.; Wang, M.; Zhang, J.; Ding, H.; Song, Y.; Zhu, Y.; Pan, Q.; Zhao, C.; Deng, H. Thiourea-assisted one-step fabrication of a novel nitrogen and sulfur co-doped biochar from nanocellulose as metal-free catalyst for efficient activation of peroxymonosulfate. *J. Hazard. Mater.* **2021**, *416*, 125796. [CrossRef]
9. Kim, D.G.; Boldbaatar, S.; Ko, S.O. Enhanced Adsorption of Tetracycline by Thermal Modification of Coconut Shell-Based Activated Carbon. *Int. J. Environ. Res. Public Health* **2022**, *19*, 13741. [CrossRef]
10. Wu, X.; Jiang, L.; Long, C.; Fan, Z. From flour to honeycomb-like carbon foam: Carbon makes room for high energy density supercapacitors. *Nano Energy* **2015**, *13*, 527–536. [CrossRef]
11. Hong, X.; Liu, Y.; Fu, J.; Wang, X.; Zhang, T.; Wang, S.; Hou, F.; Liang, J. A wheat flour derived hierarchical porous carbon/graphitic carbon nitride composite for high-performance lithium–sulfur batteries. *Carbon* **2020**, *170*, 119–126. [CrossRef]
12. Santoso, E.; Ediati, R.; Kusumawati, Y.; Bahruji, H.; Sulistiono, D.O.; Prasetyoko, D. Review on recent advances of carbon based adsorbent for methylene blue removal from waste water. *Mater. Today Chem.* **2020**, *16*, 100233. [CrossRef]
13. Song, J.; Lu, L.; Wang, J.; Li, X.; Li, J.; Wang, Q.; Du, H.; Xin, S.; Xu, L.; Yan, Q.; et al. Highly efficient nanocomposite of Y(2)O(3)@biochar for oxytetracycline removal from solution: Adsorption characteristics and mechanisms. *Bioresour. Technol.* **2023**, *385*, 129380. [CrossRef]
14. Yang, X.; Wan, Y.; Zheng, Y.; He, F.; Yu, Z.; Huang, J.; Wang, H.; Ok, Y.S.; Jiang, Y.; Gao, B. Surface functional groups of carbon-based adsorbents and their roles in the removal of heavy metals from aqueous solutions: A critical review. *Chem. Eng. J.* **2019**, *366*, 608–621. [CrossRef]
15. Zhang, L.; Song, X.; Liu, X.; Yang, L.; Pan, F.; Lv, J. Studies on the removal of tetracycline by multi-walled carbon nanotubes. *Chem. Eng. J.* **2011**, *178*, 26–33. [CrossRef]
16. Gao, Y.; Li, Y.; Zhang, L.; Huang, H.; Hu, J.; Shah, S.M.; Su, X. Adsorption and removal of tetracycline antibiotics from aqueous solution by graphene oxide. *J. Colloid Interface Sci.* **2012**, *368*, 540–546. [CrossRef]
17. Acosta, R.; Fierro, V.; Martinez de Yuso, A.; Nabarlatz, D.; Celzard, A. Tetracycline adsorption onto activated carbons produced by KOH activation of tyre pyrolysis char. *Chemosphere* **2016**, *149*, 168–176. [CrossRef]
18. Li, G.; Zhang, D.; Wang, M.; Huang, J.; Huang, L. Preparation of activated carbons from Iris tectorum employing ferric nitrate as dopant for removal of tetracycline from aqueous solutions. *Ecotoxicol. Environ. Saf.* **2013**, *98*, 273–282. [CrossRef]
19. Liao, P.; Zhan, Z.; Dai, J.; Wu, X.; Zhang, W.; Wang, K.; Yuan, S. Adsorption of tetracycline and chloramphenicol in aqueous solutions by bamboo charcoal: A batch and fixed-bed column study. *Chem. Eng. J.* **2013**, *228*, 496–505. [CrossRef]
20. Ocampo-Pérez, R.; Rivera-Utrilla, J.; Gómez-Pacheco, C.; Sánchez-Polo, M.; López-Peñalver, J.J. Kinetic study of tetracycline adsorption on sludge-derived adsorbents in aqueous phase. *Chem. Eng. J.* **2012**, *213*, 88–96. [CrossRef]
21. Wohlgemuth, S.-A.; White, R.J.; Willinger, M.-G.; Titirici, M.-M.; Antonietti, M. A one-pot hydrothermal synthesis of sulfur and nitrogen doped carbon aerogels with enhanced electrocatalytic activity in the oxygen reduction reaction. *Green Chem.* **2012**, *14*, 1515–1523. [CrossRef]
22. Tripathi, P.K.; Liu, M.; Zhao, Y.; Ma, X.; Gan, L.; Noonan, O.; Yu, C. Enlargement of uniform micropores in hierarchically ordered micro–mesoporous carbon for high level decontamination of bisphenol A. *J. Mater. Chem. A* **2014**, *2*, 8534–8544. [CrossRef]
23. Zhou, X.-L.; Zhang, H.; Shao, L.-M.; Lü, F.; He, P.-J. Preparation and Application of Hierarchical Porous Carbon Materials from Waste and Biomass: A Review. *Waste Biomass Valorization* **2020**, *12*, 1699–1724. [CrossRef]
24. Lahreche, S.; Moulefera, I.; El Kebir, A.; Sabantina, L.; Kaid, M.H.; Benyoucef, A. Application of Activated Carbon Adsorbents Prepared from Prickly Pear Fruit Seeds and a Conductive Polymer Matrix to Remove Congo Red from Aqueous Solutions. *Fibers* **2022**, *10*, 7. [CrossRef]
25. Vieira, A.L.S.; Ribeiro, R.S.; Lado Ribeiro, A.R.; Ribeiro, A.M.; Silva, A.M.T. Hollow carbon spheres for diclofenac and venlafaxine adsorption. *J. Environ. Chem. Eng.* **2022**, *10*, 107348. [CrossRef]

26. Zhang, M.; Xu, L.; Qi, C.; Zhang, M. Highly Effective Removal of Tetracycline from Water by Hierarchical Porous Carbon: Batch and Column Adsorption. *Ind. Eng. Chem. Res.* **2019**, *58*, 20036–20046. [CrossRef]
27. Ng, S.W.L.; Yilmaz, G.; Ong, W.L.; Ho, G.W. One-step activation towards spontaneous etching of hollow and hierarchical porous carbon nanospheres for enhanced pollutant adsorption and energy storage. *Appl. Catal. B Environ.* **2018**, *220*, 533–541. [CrossRef]
28. González, J.F.; Román, S.; González-García, C.M.; Nabais, J.M.V.; Ortiz, A.L. Porosity Development in Activated Carbons Prepared from Walnut Shells by Carbon Dioxide or Steam Activation. *Ind. Eng. Chem. Res.* **2009**, *48*, 7474–7481. [CrossRef]
29. Wei, H.; Deng, S.; Hu, B.; Chen, Z.; Wang, B.; Huang, J.; Yu, G. Granular bamboo-derived activated carbon for high CO_2 adsorption: The dominant role of narrow micropores. *ChemSusChem* **2012**, *5*, 2354–2360. [CrossRef]
30. Cuong, D.V.; Liu, N.L.; Nguyen, V.A.; Hou, C.H. Meso/micropore-controlled hierarchical porous carbon derived from activated biochar as a high-performance adsorbent for copper removal. *Sci. Total Environ.* **2019**, *692*, 844–853. [CrossRef]
31. Fu, Y.; Shen, Y.; Zhang, Z.; Ge, X.; Chen, M. Activated bio-chars derived from rice husk via one- and two-step KOH-catalyzed pyrolysis for phenol adsorption. *Sci. Total Environ.* **2019**, *646*, 1567–1577. [CrossRef]
32. Lin, Y.; Li, F.; Li, X.; Zhao, H.; Liu, G. Multifunctional Template Prepares N-, O-, and S-Codoped Mesoporous 3D Hollow Nanocage Biochar with a Multilayer Wall Structure for Aqueous High-Performance Supercapacitors. *ACS Appl. Energy Mater.* **2023**, *6*, 2265–2275. [CrossRef]
33. Zhao, L.; Cao, X.; Masek, O.; Zimmerman, A. Heterogeneity of biochar properties as a function of feedstock sources and production temperatures. *J. Hazard. Mater.* **2013**, *256–257*, 1–9. [CrossRef] [PubMed]
34. Chen, T.; Luo, L.; Deng, S.; Shi, G.; Zhang, S.; Zhang, Y.; Deng, O.; Wang, L.; Zhang, J.; Wei, L. Sorption of tetracycline on H_3PO_4 modified biochar derived from rice straw and swine manure. *Bioresour. Technol.* **2018**, *267*, 431–437. [CrossRef] [PubMed]
35. Sevilla, M.; Diez, N.; Fuertes, A.B. More Sustainable Chemical Activation Strategies for the Production of Porous Carbons. *ChemSusChem* **2021**, *14*, 94–117. [CrossRef] [PubMed]
36. Wang, J.; Kaskel, S. KOH activation of carbon-based materials for energy storage. *J. Mater. Chem.* **2012**, *22*, 23710–23725. [CrossRef]
37. Wang, J.; Lei, S.; Liang, L. Preparation of porous activated carbon from semi-coke by high temperature activation with KOH for the high-efficiency adsorption of aqueous tetracycline. *Appl. Surf. Sci.* **2020**, *530*, 147187. [CrossRef]
38. Ouyang, T.; Zhang, T.; Wang, H.; Yang, F.; Yan, J.; Zhu, K.; Ye, K.; Wang, G.; Zhou, L.; Cheng, K.; et al. High-throughput fabrication of porous carbon by chemical foaming strategy for high performance supercapacitor. *Chem. Eng. J.* **2018**, *352*, 459–468. [CrossRef]
39. Cheng, F.; Li, X. Preparation and Application of Biochar-Based Catalysts for Biofuel Production. *Catalysts* **2018**, *8*, 346. [CrossRef]
40. Gan, Y.X. Activated Carbon from Biomass Sustainable Sources. *C* **2021**, *7*, 39. [CrossRef]
41. Song, G.; Deng, R.; Yao, Z.; Chen, H.; Romero, C.; Lowe, T.; Driscoll, G.; Kreglow, B.; Schobert, H.; Baltrusaitis, J. Anthracite coal-based activated carbon for elemental Hg adsorption in simulated flue gas: Preparation and evaluation. *Fuel* **2020**, *275*, 117921. [CrossRef]
42. Schott, J.A.; Do-Thanh, C.-L.; Shan, W.; Puskar, N.G.; Dai, S.; Mahurin, S.M. FTIR investigation of the interfacial properties and mechanisms of CO_2 sorption in porous ionic liquids. *Green Chem. Eng.* **2021**, *2*, 392–401. [CrossRef]
43. Song, X.; Zhang, Y.; Chang, C. Novel Method for Preparing Activated Carbons with High Specific Surface Area from Rice Husk. *Ind. Eng. Chem. Res.* **2012**, *51*, 15075–15081. [CrossRef]
44. Zhang, Z.; Li, Y.; Ding, L.; Yu, J.; Zhou, Q.; Kong, Y.; Ma, J. Novel sodium bicarbonate activation of cassava ethanol sludge derived biochar for removing tetracycline from aqueous solution: Performance assessment and mechanism insight. *Bioresour. Technol.* **2021**, *330*, 124949. [CrossRef]
45. Chi, H.; Xu, K.; Wu, X.; Chen, Q.; Xue, D.; Song, C.; Zhang, W.; Wang, P. Effect of acetylation on the properties of corn starch. *Food Chem.* **2008**, *106*, 923–928. [CrossRef]
46. Leblanc, N.; Saiah, R.; Beucher, E.; Gattin, R.; Castandet, M.; Saiter, J.M. Structural investigation and thermal stability of new extruded wheat flour based polymeric materials. *Carbohydr. Polym.* **2008**, *73*, 548–557. [CrossRef] [PubMed]
47. Silva, T.L.; Ronix, A.; Pezoti, O.; Souza, L.S.; Leandro, P.K.T.; Bedin, K.C.; Beltrame, K.K.; Cazetta, A.L.; Almeida, V.C. Mesoporous activated carbon from industrial laundry sewage sludge: Adsorption studies of reactive dye Remazol Brilliant Blue R. *Chem. Eng. J.* **2016**, *303*, 467–476. [CrossRef]
48. Zhu, G.; Liu, Q.; Cao, F.; Qin, Q.; Jiao, M. Silkworm cocoon derived N, O-codoped hierarchical porous carbon with ultrahigh specific surface area for efficient capture of methylene blue with exceptionally high uptake: Kinetics, isotherm, and thermodynamics. *RSC Adv.* **2019**, *9*, 33872–33882. [CrossRef]
49. Kuśmierek, K.; Świątkowski, A.; Skrzypczyńska, K.; Błażewicz, S.; Hryniewicz, J. The effects of the thermal treatment of activated carbon on the phenols adsorption. *Korean J. Chem. Eng.* **2017**, *34*, 1081–1090. [CrossRef]
50. Cheng, M.; Zhang, Y.; Lai, B.; Wang, L.; Yang, S.; Li, K.; Wang, D.; Wu, Y.; Chen, G.-H.; Qian, J. Nitrogen and phosphorus co-doped porous carbons (NPCs) for peroxydisulfate (PDS) activation towards tetracycline degradation: Defects enhanced adsorption and non-radical mechanism dominated by electron transfer. *Chem. Eng. J.* **2023**, *455*, 140615. [CrossRef]
51. Eckmann, A.; Felten, A.; Mishchenko, A.; Britnell, L.; Krupke, R.; Novoselov, K.S.; Casiraghi, C. Probing the nature of defects in graphene by Raman spectroscopy. *Nano Lett.* **2012**, *12*, 3925–3930. [CrossRef] [PubMed]
52. Rong, H.; Ryu, Z.; Zheng, J.; Zhang, Y. Influence of heat treatment of rayon-based activated carbon fibers on the adsorption of formaldehyde. *J. Colloid Interface Sci.* **2003**, *261*, 207–212. [CrossRef]

53. Yu, F.; Pan, J.; Li, Y.; Yang, Y.; Zhang, Z.; Nie, J.; Ma, J. Batch and continuous fixed-bed column adsorption of tetracycline by biochar/MOFs derivative covered with κ-carrageenan/calcium alginate hydrogels. *J. Environ. Chem. Eng.* **2022**, *10*, 107996. [CrossRef]
54. Jang, H.M.; Kan, E. Engineered biochar from agricultural waste for removal of tetracycline in water. *Bioresour. Technol.* **2019**, *284*, 437–447. [CrossRef] [PubMed]
55. Yang, Z.; Xing, R.; Zhou, W. Adsorption of ciprofloxacin and Cu^{2+} onto biochars in the presence of dissolved organic matter derived from animal manure. *Environ. Sci. Pollut. Res. Int.* **2019**, *26*, 14382–14392. [CrossRef] [PubMed]
56. Peng, X.; Hu, F.; Huang, J.; Wang, Y.; Dai, H.; Liu, Z. Preparation of a graphitic ordered mesoporous carbon and its application in sorption of ciprofloxacin: Kinetics, isotherm, adsorption mechanisms studies. *Microporous Mesoporous Mater.* **2016**, *228*, 196–206. [CrossRef]
57. Mozaffari Majd, M.; Kordzadeh-Kermani, V.; Ghalandari, V.; Askari, A.; Sillanpaa, M. Adsorption isotherm models: A comprehensive and systematic review (2010–2020). *Sci. Total Environ.* **2022**, *812*, 151334. [CrossRef]
58. Rout, D.R.; Jena, H.M.; Baigenzhenov, O.; Hosseini-Bandegharaei, A. Graphene-based materials for effective adsorption of organic and inorganic pollutants: A critical and comprehensive review. *Sci. Total Environ.* **2023**, *863*, 160871. [CrossRef]
59. El Hassani, A.A.; Tanji, K.; El Mrabet, I.; Fahoul, Y.; El Gaidoumi, A.; Benjelloun, A.T.; Sfaira, M.; Zaitan, H.; Kherbeche, A. A combined molecular dynamics simulation, DFT calculations, and experimental study of the adsorption of Rhodamine B dye on kaolinite and hydroxyapatite in aqueous solutions. *Surf. Interfaces* **2023**, *36*, 102647. [CrossRef]
60. Mohammadzadeh, A.; Kadhim, M.M.; Taban, T.Z.; Baigenzhenov, O.; Ivanets, A.; Lal, B.; Kumar, N.; Hosseini-Bandegharaei, A. Adsorption performance of Enterobacter cloacae towards U(VI) ion and application of Enterobacter cloacae/carbon nanotubes to preconcentration and determination of low-levels of U(VI) in water samples. *Chemosphere* **2023**, *311*, 136804. [CrossRef]
61. Oh, W.D.; Zaeni, J.R.J.; Lisak, G.; Lin, K.A.; Leong, K.H.; Choong, Z.Y. Accelerated organics degradation by peroxymonosulfate activated with biochar co-doped with nitrogen and sulfur. *Chemosphere* **2021**, *277*, 130313. [CrossRef]
62. Pham, V.L.; Kim, D.G.; Ko, S.O. Cu@Fe_3O_4 core-shell nanoparticle-catalyzed oxidative degradation of the antibiotic oxytetracycline in pre-treated landfill leachate. *Chemosphere* **2018**, *191*, 639–650. [CrossRef] [PubMed]
63. Pham, V.L.; Kim, D.G.; Ko, S.O. Advanced oxidative degradation of acetaminophen by carbon catalysts: Radical vs non-radical pathways. *Environ. Res.* **2020**, *188*, 109767. [CrossRef] [PubMed]
64. He, D.; Zhu, K.; Huang, J.; Shen, Y.; Lei, L.; He, H.; Chen, W. N, S co-doped magnetic mesoporous carbon nanosheets for activating peroxymonosulfate to rapidly degrade tetracycline: Synergistic effect and mechanism. *J. Hazard. Mater.* **2022**, *424*, 127569. [CrossRef] [PubMed]
65. Wei, Z.; Hou, C.; Gao, Z.; Wang, L.; Yang, C.; Li, Y.; Liu, K.; Sun, Y. Preparation of Biochar with Developed Mesoporous Structure from Poplar Leaf Activated by KHCO(3) and Its Efficient Adsorption of Oxytetracycline Hydrochloride. *Molecules* **2023**, *28*, 3188. [CrossRef]
66. Yang, J.-G.; Bai, X.-J.; Wang, Y.-L. The preparation of synthetic graphite materials with hierarchical pores from lignite by one-step impregnation and their characterization as dye absorbents. *RSC Adv.* **2019**, *9*, 12737–12746. [CrossRef]
67. Xu, K.; Yang, X.; Ruan, L.; Qi, S.; Liu, J.; Liu, K.; Pan, S.; Feng, G.; Dai, Z.; Yang, X.; et al. Superior Adsorption and Photocatalytic Degradation Capability of Mesoporous $LaFeO_3$/g-C_3N_4 for Removal of Oxytetracycline. *Catalysts* **2020**, *10*, 301. [CrossRef]
68. Li, Q.; Zhao, S.; Wang, Y. Mechanism of Oxytetracycline Removal by Coconut Shell Biochar Loaded with Nano-Zero-Valent Iron. *Int. J. Environ. Res. Public Health* **2021**, *18*, 13107. [CrossRef]
69. Xin, Y.; Zhang, P.; Shen, J.; Ren, S. Development of Vitamin B6-Mediated Biochar with Nano Zero-Valent Iron Coating for Oxytetracycline Removal through Adsorption and Degradation under Harsh Acidic Conditions. *Water* **2022**, *14*, 2734. [CrossRef]
70. Kumar, R.; Oves, M.; Ansari, M.O.; Taleb, M.A.; Baraka, M.A.E.; Alghamdi, M.A.; Makishah, N.H.A. Biopolymeric Ni(3)S(4)/Ag(2)S/TiO(2)/Calcium Alginate Aerogel for the Decontamination of Pharmaceutical Drug and Microbial Pollutants from Wastewater. *Nanomaterials* **2022**, *12*, 3642. [CrossRef]
71. Kumar, R.; Ansari, M.O.; Taleb, M.A.; Oves, M.; Barakat, M.A.; Alghamdi, M.A.; Al Makishah, N.H. Integrated Adsorption-Photocatalytic Decontamination of Oxytetracycline from Wastewater Using S-Doped TiO_2/WS_2/Calcium Alginate Beads. *Catalysts* **2022**, *12*, 1676. [CrossRef]